JOM, Vol. 67, No. 8, 2015
DOI: 10.1007/s11837-015-1448-y

Evaluation of Incoherent Interface Strength of Solid-State-Bonded Ti64/Stainless Steel Under Dynamic Impact Loading

DEVENDRA VERMA,[1] JOGENDER SINGH,[2] AMIT H. VARMA,[3] and VIKAS TOMAR[1,4]

1.—School of Aeronautics and Astronautics, Purdue University, West Lafayette, IN 47907, USA. 2.—Department of Materials Science and Engineering, The Pennsylvania State University, University Park, PA 16801, USA. 3.—School of Civil Engineering, Purdue University, West Lafayette, IN 47907-2051, USA. 4.—e-mail: tomar@purdue.edu

Ti/steel interfaces are produced using field-assisted sintering technology, a technique known to bring about full consolidation of materials using much lower sintering temperatures and durations. The interface thickness is verified using the energy-dispersive x-ray analysis exhibiting the extent of diffusion in interface regions. The interface mechanical strength is characterized using dynamic indentation experiments at strain rates approaching 400 s^{-1}. The experiments were conducted on the interfaces within the spatial error tolerance of less than 3 μm. The measurements of dynamic hardness values, strain rates, and plastic-residual depths were correlated to show the relation of interface mechanical strength with the bulk-phase mechanical strength properties of Ti and steel. The Johnson–Cook model is fitted to the obtained interface normal stress–normal strain data based on the nanoimpact experiments. The coefficient of restitution in the mechanical loading and its dependence on the interface dynamic hardness and interface impact velocity validate the experimental results. The results show that interfacial properties are affected by the rate of loading and are largely dependent upon the interface structural inhomogeneity.

INTRODUCTION

Dynamic material damage occurs under a variety of loading conditions such as sand particle erosion, shot peening, and projectile impact. Although significant research effort has focused on developing polycrystalline material constitutive laws under impact, the dynamic interface constitutive behavior remains largely uninvestigated.[1] Recent progress in dynamic loading failure investigations has shown that interfaces play a significant part in determining material failure.[1] The current work focuses on investigating interface failure under dynamic impact loading. Several material constitutive models have been developed to show the effect of strain rate on the dynamic strength of materials.[2–5] During the impact loading events, stress waves or shock waves propagate inside the impacted bodies and large inelastic deformations develop. The high-strain-rate deformation behavior is accompanied by both plastic deformation and twin-dislocation interactions that vary with the crystal unit cell structure, such as the hexagonal close-packed (hcp) unit cell in the case of titanium alloys.[6] Because of the complexity of the deformations at higher strain rates, the development of material model needs intelligently designed experiments. The split Hopkinson bar experiment is a popular method to conduct high-strain-rate experiments in the tensile and compression mode to model the dynamic material behavior.[7] The experimental procedure involves impact on bulk material. On the other hand, the development of nanoindentation techniques in the last decades have allowed us to model the site-specific behavior such as at the interface between two materials at higher strain rates.[8] The current work focuses on using such technique.

In aerospace, nuclear, and chemical industries, titanium alloys have wide application and thus the effective utilization of titanium alloys needs the development of reliable joining techniques, especially joining techniques of titanium alloys to other

(Published online May 27, 2015)

significant materials such as stainless steel, which also have wide application in industry.[9] Several titanium-based interfaces have been investigated in the literature such as the nanostructured surface of Ti64 in orthopedics[10] and interfaces between Ti and different steel alloys such as microduplex stainless steel, which is a diffusion-bonded joint using Ni alloy as an intermediate materials[9] or nickel alloy as an interlayer.[11] The interface between aerospace alloys: Ti-6AL-4V alloy (Ti64) and 304 stainless steel (SS)[9–21] has been investigated thoroughly in materials science because of their prevalent applications in aerospace and automotive industries. The most common practice is to produce such interface using direct solid-state diffusion bonding. Diffusion bonding has proven to be near-net shape-forming process for simultaneous joining and manufacturing of Ti alloy materials without gross macroscopic distortion and with minimum dimensional tolerances, as Ti alloy exhibits both the superplasticity and the diffusion bonding under same conditions.[20] However, direct diffusion bonding of Ti64/stainless steel leads to problems such as intermetallic brittle phase formation and residuals stress at the interfaces. As a result, the bond strength of such interfaces drops due to the increase in the interface thickness. The manufacturing process variables affect interface properties to a great extent. Through vacuum thermal exposure, it has been established that the interface growth is controlled by diffusion. The diffusion of Ti, Al, and V mainly relies on vacancies, dislocations, and grain boundaries during hot pressing.[21] The thicknesses of different reaction products at the bond interface play an important role in determining the mechanical properties of the joints. The residual stress of bonded joints increases with bonding temperatures and time.[18] The extent of mass transfer depends on the bonding temperature. The increase in the bonding temperature drives more atoms to migrate across the interface, which is responsible for widening the reaction layers. An increase in bonding temperature also promotes the volume fraction of intermetallic compounds; hence, the bond strength drops.[16,17] In the case of diffusion bonding of dissimilar materials, an interlayer inserted between substrates is often necessary to prevent the formation of intermetallic compound and to reduce the residual stress in the joints. The interlayer used in titanium alloy and stainless steel joints has several advantages, such as low residual stress in the indirect bonded joint because the interlayer material serves as a buffer for the low pressure required within the bonding zone during a joining process.

To understand the underlying mechanisms and the structure of interfaces along with their mechanical strength, characterization techniques with sufficient resolution are needed. However, until recently, the investigation of material deformation with electron microscopy has been limited to bulk phase properties. In this work, the interface properties at Ti/steel interfaces are probed by nanoscale impact experiments. The novelty of the experiments lies in the fact that the impacts are precisely at the interfaces in the precision range of nanometers to micrometers as required by the material microstructure. The probe used for impact has tip radius of 30 nm. This tip impacts at the interfaces, thus making sure that energy from the impact is delivered at the interfacial region. The strain rates during impacts are calculated and are correlated with the damage occurring during the impact event. The energy of impact is also calculated for impacts during each loading cycle and is related to the interface damage. Such precise correlations are not possible during impacts with bigger probes where the entire material microstructure is under the loading. The impact velocity and rebound velocities during impacts are measured to calculate the coefficient of restitution, which is related to the dynamic hardness of the material and the strain rate during impacts. The impact stress–strain data from experiments are fitted to the Johnson–Cook (JC) constitutive model to define the material behavior at high strain rates. It is important to point out that the current experimental setup, while imparting high degree of spatial accuracy, is based on uniaxial measurements. Indentation experiment measurements are also restricted by in-plane constraints. Within such limitation, the present work offers a first step in developing a comprehensive multiaxial damage-plasticity-fracture model for interface behavior. The interface behavior is modeled using the JC multiaxial plasticity model, and the dynamic high-strain-rate nanoindentation data are used to extract the interface material effective stress–plastic strain behavior, which is further used to calculate parameters of the JC multiaxial model. Inherent in this development are the assumptions that the interface material follows pressure-independent behavior and that there is no damage initiation in the range of testing and calibration. Because the multiaxial plasticity model is assumed to be pressure independent, the required numbers of tests for parameter extraction are significantly reduced. This assumption is later verified based on the predicted constitutive behavior of interfaces using the fitted JC model. The impact stress–strain behavior measured and discussed in this article form one of the unique inputs required to develop and calibrate the multiaxial model. Additional experiments will be designed and conducted to enhance the fidelity of the calibration of the multiaxial model. For example, the nanomechanical Raman spectroscopy approach developed by the authors will be used.[22–24]

METHODS

Material

Ti-6Al-4V/304 stainless steel interfaces were prepared by compressing Ti64 and stainless steel

together at 45 MPa at 975°C for 10 min. Sintering experiments were carried out in a field-assisted sintering technology (FAST) 250-ton system (Fig. 1; FCT Systeme GmbH, Frankenblick, Germany). The Ti/steel interface was processed using FAST, a technique known to bring about full consolidation of materials using much lower sintering temperatures and durations. The sintering was carried out by concurrently applying temperature, pressure and high current density. The maximum load capability of FAST is 250 tons with maximum displacement of 300 mm. The allowable temperature ranges are from room temperature up to 2400°C. The scanning electron microscope (SEM) image of the final sample is shown in Fig. 2. In bimetallic composites, an interlayer is inserted to reduce the effects of intermetallic brittle phase formation and to avoid residual stresses at the interface. The thickness of the interlayer inserted between the two materials is in the range of 5–50 μm. The thin interlayer becomes diffused in both phases at the interface; thus, it does not produce additional interfaces. The tip of the indenter in the dynamic indentations was 30 nm. It enables to perform indents exactly at the interface. The indentation setup is equipped with a microscope that is used to examine the indentation area before experiments and to choose specific sites to perform impacts.

Fig. 1. Photograph showing FCT's 250-ton FAST system.

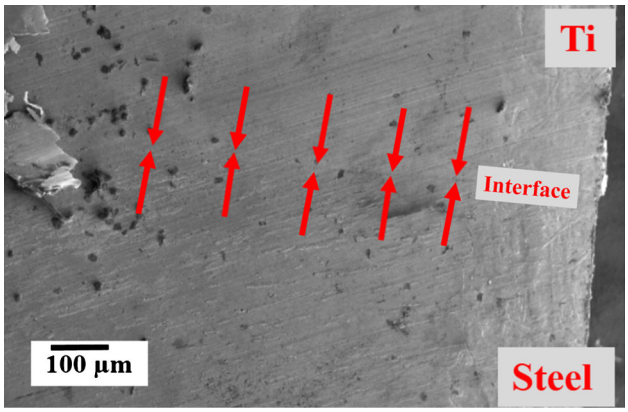

Fig. 2. SEM image showing Ti/steel interface.

Experimental Procedure: Dynamic Indentation

The dynamic indentations were performed using the high-strain-rate impact schedule of Micro Materials (Wrexham, U.K.).[25] The experimental setup consists of the three-dimensional stage to mount the sample that allows it to move in all x, y, and z directions. The indents were performed with a cube-corner indenter. The indenter is mounted on a pendulum that is hanging vertically on frictionless springs to let it move freely. The force on the pendulum is applied through the electromagnets as shown in Fig. 3. The depth of the indent is measured as function of change in the capacitance of the plates attached at the back of the indenter. It allows for high accuracy in depth measurements. The additional force for high-strain-rate impacts is provided with the help of a solenoid situated at the lower part of the pendulum. Load and depth calibrations were performed before the experiments, and the instrument was kept inside a thermally stable chamber on a vibration isolation table. During the impacts, the force is applied with both electromagnets and the solenoid to the pendulum, which means it is being pulled at both ends. At the instant of impact, the solenoid is turned off, which releases the pendulum and it hits the sample. The load of the dynamic indentation is predefined in the experiment. The initial impact and the subsequent rebound depth versus time history is also recorded. These data are further analyzed to calculate the dynamic hardness, maximum strain, strain rate, impact depth, stress at maximum depth, stress rate,

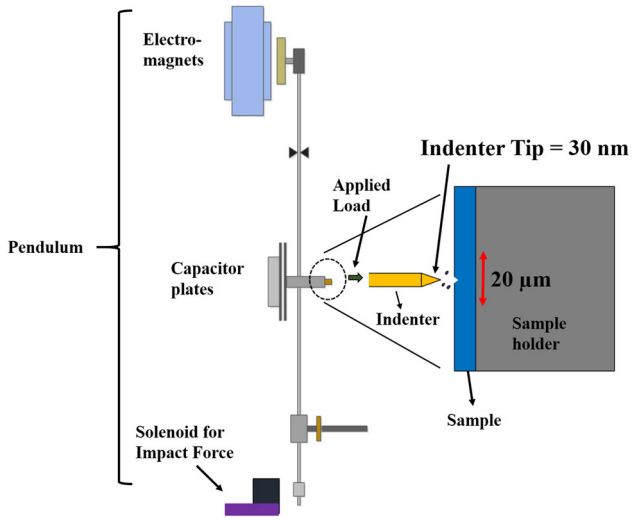

Fig. 3. Schematic of instrument setup for dynamic indentation tests.

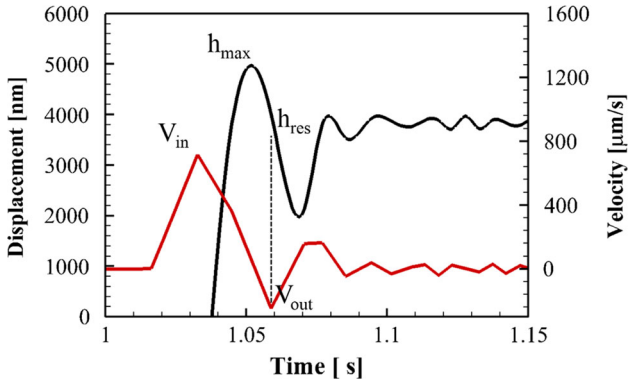

Fig. 4. Data output from high-strain-rate impact tests, depth data marked with h_{max} and velocity data marked with V_{in}.

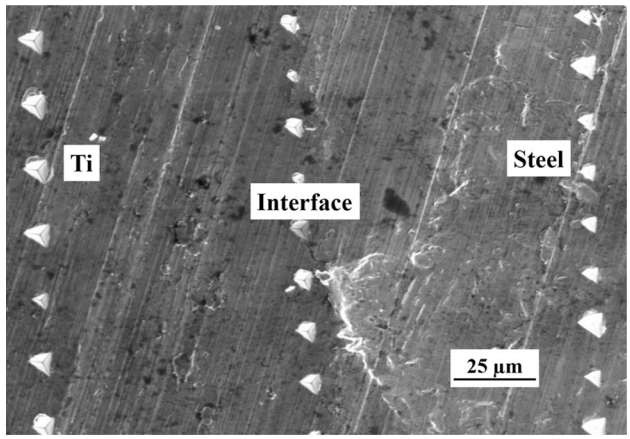

Fig. 5. Postimpact SEM image of Ti/steel surface.

impact velocity at the time of impact and in rebound stage, coefficient of restitution, and energy absorbed during indentation.

From its initial stationary solenoid position, the indenter position is monitored continuously as a function of time t, including the initial impact trajectory and the initial rebound from the material surface.[8] During single-impact experiments, a typical depth versus time history is shown in Fig. 4. The velocity of the indenter can be calculated as the first derivative of the response marked with V_{in} in Fig. 4. The maximum depth, the initial contact velocity, the outgoing velocity, and the residual depth are calculated from these data. The residual depth is the position at the point of detachment from the sample on the first rebound. The strain rate $\dot{\varepsilon}$ of the impact changes with the depth of the impact. An average strain rate characterizing the impact can be approximated by the expression:

$$\dot{\varepsilon} \approx \frac{V_{in}}{h_{max}}, \tag{1}$$

where h_{max} is the maximum depth and V_{in} is the maximum velocity. The kinetic energy consumed in the plastic work done by indenter is given as:[26,27]

$$\frac{m\left(V_{in}^2 - V_{out}^2\right)}{2} = \int_0^{h_{res}} P\mathrm{d}h, \tag{2}$$

where m is the mass of pendulum, P is the indentation load, V_{out} is the outgoing velocity of indenter, and h_{res} is the residual depth of the impact. The projected area for the cube corner indenter is $A_c = ch^2$ with $c = 2.59$. The effective dynamic hardness H_d is then defined as derived by Somekawa and Schuh:[27]

$$H_d = \frac{3m\left(V_{in}^2 - V_{out}^2\right)}{2ch_{res}^3}. \tag{3}$$

The strain rate in the dynamic indentations was in the range of 10–400 s^{-1}. These strain rates in the current experiment depend on the maximum load applied at the impacts. The highest load was applied to observe the behavior of material under the highest deformation state. The impacts were conducted at the interface of the two metals and the in the bulk phase of both materials.

SEM and Energy-Dispersive X-Ray (EDX)

SEM images were obtained by FEI Nova nanoSEM (FEI Company, Hillsboro, OR). The working distance for Nova SEM was 5 mm with 5.00 kV accelerating voltage in high vacuum chamber. EDX analysis was performed using FEI Quanta three-dimensional field-emission gun dual-beam SEM. The working distance for Quanta SEM was 10 mm with 20.00 kV accelerating voltage in high vacuum chamber and cryogenic environment.

RESULTS AND DISCUSSION

EDX Analysis of Diffusion-Bonded Joints

The EDX analysis was conducted to verify the site postimpact. Figure 5 shows an SEM image of the impact marks on the surface of the sample. The width of the indent marks is in the range of 1–5 μm. The depths of the indents were in the range of 1–4 μm. The sites of the indents at the interface were confirmed by the elemental mapping of the surface as shown in Fig. 6. Figure 6a shows the impact area in the interfaces region, which is further verified in the elemental spectrum shown in Fig. 6b. Figure 7 illuminates the diffused region where Fe and Ti phases are diffused into each other. The individual element mapping of Ti and Fe is shown in Fig. 7a and b, respectively. Stainless steel has close-packed face-centered cubic structure; hence, the extent of diffusion of Ti elements across the bond line is limited as evident from Fig. 7a, where Ti elements are mostly in the left region of the image. On the contrary, owing to more open crystallography of body-centered cubic matrix, Fe atoms can penetrate further into the titanium lattice as shown in Fig. 7b; Fe elements are present

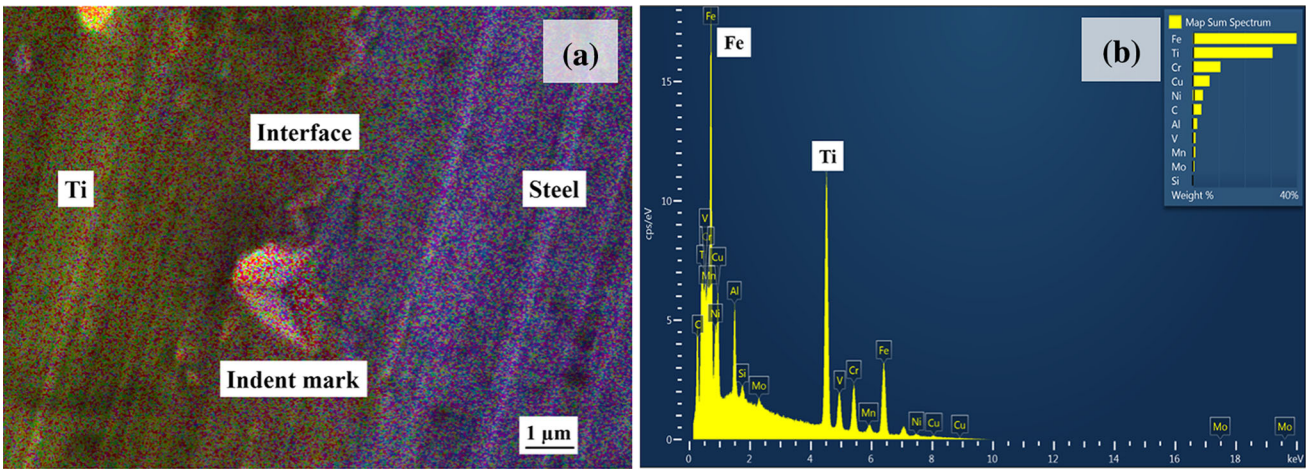

Fig. 6. (a) EDX image with indent mark and (b) elemental spectrum.

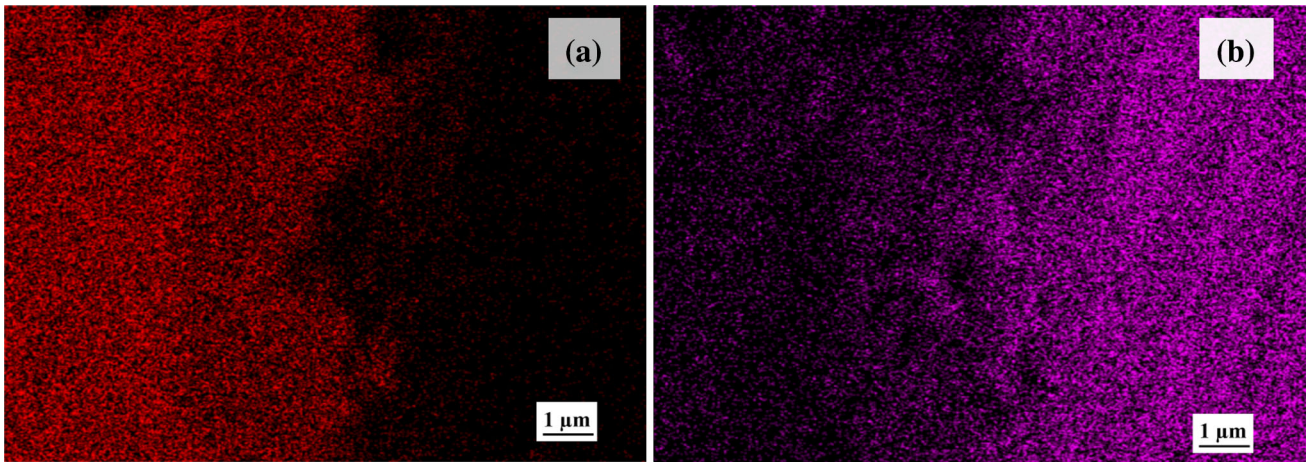

Fig. 7. EDX elemental map of (a) Ti and (b) Fe (steel).

also in the left region of the image. The samples were prepared at a temperature of 975°C, which is closer to the beta phase transition temperature[28] of Ti64, and the diffusion of the chemical species becomes easier through the interlayer; i.e., Ti can migrate to Fe side and vice versa.

Mechanical Properties of Diffusion-Bonded Joints

The dynamic indentation data is analyzed to calculate the dynamic hardness of the specimen interfaces, strain rate during impact, depth during impact, stress at maximum depth, velocity of impact, and energy absorbed during impact. These measurements are highly variable, and their uncertainty increases with dynamic or strain-rate effects.[29] Here, the uncertainty is the change in the measurement of one parameter with respect to change in the other parameter. The variability in the experimental dynamic indentation data results

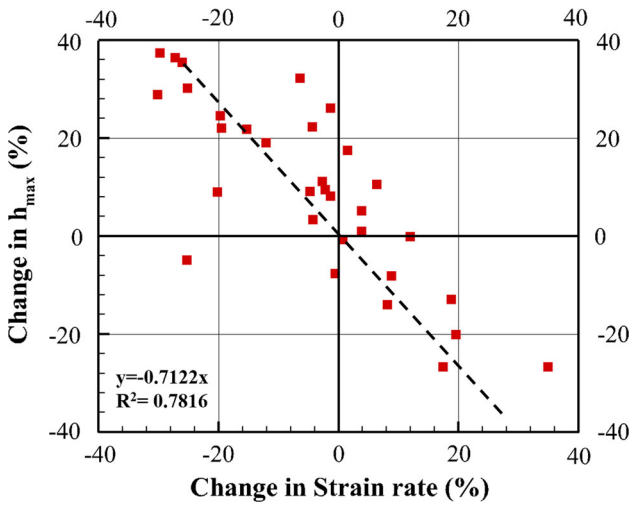

Fig. 8. Influence of strain rate on the measured maximum impact depth.

Table I. Correlation coefficients for the dynamic hardness with respect to strain rate, plastic depth of impact, residual depth of impact, stress rate, and energy absorbed at impact at interface region, Ti and steel

H_{dyn}	Strain rate	$h_{plastic}$	h_{res}	Stress Rate	$E_{absorbed}$
Ti/steel	0.73931	−0.47867	−0.77260	0.50780	0.67832
Ti	0.93366	−0.80457	−0.76827	0.92681	0.53431
Steel	0.90321	−0.70209	−0.83883	0.87092	0.65154

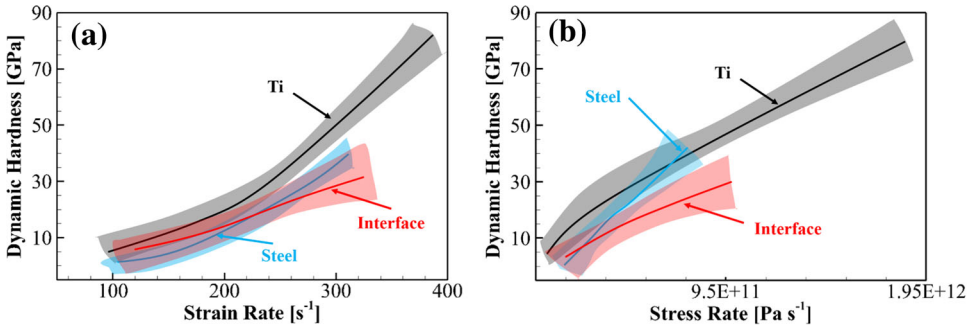

Fig. 9. Trend of dynamic hardness on Ti/steel interfaces with (a) strain rate and (b) stress rate.

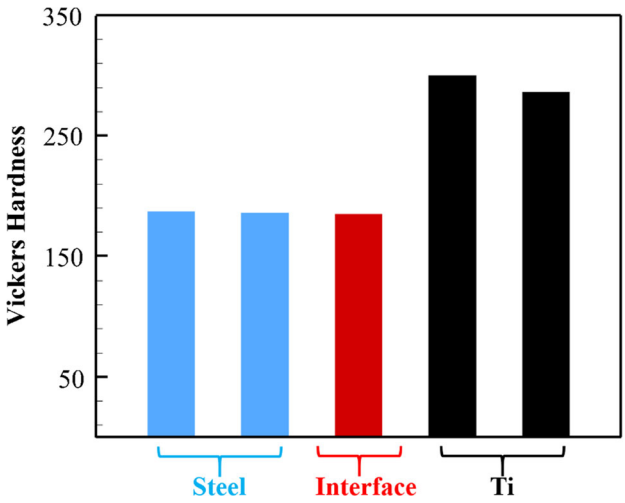

Fig. 10. Trend of Vickers hardness in low-strain-rate experiments on Ti/steel interfaces.

from uncertainties associated with the testing conditions and loading apparatus. The measured values of dynamic hardness, strain impact, impact depth, and so on reflect this uncertainty in the loading and measurement, as well as the fundamental composition and behavior of the interface material. Figure 8 shows the influence of strain rate on the resulting uncertainty in impact depth. The measured properties are therefore presented as a function of strain rates in the analysis given in the following sections.

A check was performed on the data for the statistical analysis. The data for the dynamic indentation were analyzed using statistical analysis software SAS (SAS Institute Inc., Cary, NC). A program was written in SAS to check the correlation between the dynamic hardness and the parameters of the experiment. Table I shows the correlation coefficients of the dynamic hardness corresponding to the strain rate, plastic depth defined by maximum depth of impact, residual depth, stress rate, and energy absorbed during impact. The stress rate was calculated as change in the stress from the initial point of contact to the maximum depth. The stress was calculated at the maximum depth and multiplied by the strain rate to find the stress rate. Dynamic hardness shows a strong positive correlation (>90) with the strain rate and stress rate for the Ti and Fe phase, but it shows a relatively weaker correlation for the interface region. Similarly, high positive correlations are shown for the stress rates but lower correlations at the interface region. The depth of impact shows similar negative correlations for residual depths but a lower negative correlation for the plastic depth in the case of the interface region. In all cases, the absorbed energy during the impacts shows correlations in the similar range. These correlations are evidence to the fact that constitutive behavior of material in interface regions is different that of the bulk material phases.

The dynamic hardness has a positive correlation to the strain rate and stress rate, whereas it has a negative correlation with the plastic and residual depth of the. Figure 9 shows that in the case of Ti/steel samples, the hardness of the interface region starts at a higher position than steel at lower strain rates, but with the increase in the strain rate, it is less than the bulk material.

The interface hardness is closer to the hardness of steel as seen from the 95% confidence interval bounds in Fig. 9 showing a deviation from the trends of bulk phases at higher strain rates. It shows the same trend for the hardness of these samples from quasi-static experiments as shown in Fig. 10 where the hardness of the interface regions falls within the same range as steel. As shown, the quasi-static hardness value based on standard Vicker's test is significantly higher than the dynamic hardness values. The length scale of measurement in Vickers test is a few hundred micrometers. The length scale in the case of the nanoimpact experiments is 1–5 μm. This shows that the current nanoimpact test is better suited to evaluate the hardness of the material at the nanoscale and microscale microstructure such as at the interfaces.

Johnson–Cook Constitutive Model

Different dynamic strength models are available in the literature that are applicable to varying strain rate range and loading conditions. One example is Steinberg–Guinan (SG)[2] model for the one-dimensional dynamic deformation response of isotropic materials subjected to longitudinal plate impact experiments. The SG model cannot be used to characterize the instantaneous state of the material nor capture its evolving history. This model is useful for modeling many aspects of plate-impact experiments at high rates including melting, strain hardening, and elastic–plastic wave interactions. The JC[3] dynamic strength model is a popular method that gives an empirical description of the flow stress dependence on effective plastic strain, strain rate, and temperature. The JC model is the product of empirical relations used to describe strain hardening, strain-rate hardening, and thermal softening up to strain rates of 10^4 s^{-1}. Steinberg and Lund (SL)[5] proposed a model to address limitations of the SG model, such as the inability to capture strain-rate-dependent material behavior that directly incorporates a rate-dependent strength and can be used to model strain rates as low as 10^{-4} s^{-1}. Similarly, Zerilli and Armstrong (ZA) [4] proposed a constitutive model based on a partitioning the total strength into contributions from an athermal part, a thermal part, and a grain-size-dependent part. It can model the behavior of material for strain rates higher than 10^4 s^{-1}. The mechanical threshold stress[30] model is based on using a single internal state variable to describe the evolving structure of the material. This model fits within the context of internal state variable theory of viscoplastic deformation for a strain rate up to 10^4 s^{-1}, but it is more complex to apply. For the high strain rates encountered in shock loading $\geq 10^5$ s^{-1}, the SG and SL models are the simplest models to implement. In the current case, however, with strain rates lower than 10^4 s^{-1}, the JC model is the most applicable model because of the least number of material parameters used in the model. The JC constitutive model[3] is an empirical model, where equivalent stress is given as a function of the strain, and the strain rate and temperature are as follows:

$$\sigma = [A + B\varepsilon^n][1 + C \ln \dot{\varepsilon}][1 - T^{*m}], \tag{4}$$

where σ is the equivalent stress, ε is the effective plastic strain, and $\dot{\varepsilon}$ is the normalized effective plastic strain rate (normalized to strain rate of 1.0 s^{-1} in the current case). T^* is defined as $T^* = (T - T_r)/(T_m - T_r)$, where T_r is room temperature, T_m is the melting temperature, and T is the absolute temperature. A, B, n, C, and m are material constants. In the current case, the temperature during the experiments is the room temperature, so Eq. 5 simplifies to

$$\sigma = [A + B\varepsilon^n][1 + C \ln \dot{\varepsilon}]. \tag{5}$$

Table II. Material parameters from the JC model

	A (MPa)	*B* (MPa)	*C*	*n*
Ti/steel interface	111	3,400	0.0010	0.54
Ti	676	5,750	0.0012	0.61
Steel	156	1,950	0.0011	0.20

The stress–strain data from the dynamic indentation experiments was fitted with the JC model to find the material constants. During the dynamic indentation experiments, the stress data for the strain from 0.2 to 0.4 is measured. The strain in the indention with spherical indenters is defined in the literature as the contact radius divided by the radius of the indenter with a constant to take into account the experimental conditions.[31,32] A cube corner indenter is used in the current experiment, so to take into account the three dimensional effects, the strain is defined as the residual area divided by the maximum area of contact during the impacts. The JC model in Eq. 5 is fitted on this range of strain considering an average strain rate of 300 s^{-1} during the experiments. The calculated material parameters are given in Table II. The fitted curves from the JC model are given in Fig. 11. Table II shows that the yield stress parameter (A) for the interface is lower than the Ti and steel. But the values of parameter B and n are higher than the steel phase. This behavior is particularly of interest in the interfacial region showing that although it starts to yield at yield stresses comparable with steel, it has a higher strain-hardening rate. The deformation mechanisms of materials at the high strain regime depend on the microstructure, strain rates, dislocation movements, and grain boundaries and orientations.[33] The current analysis shows dynamic indentation as a tool to capture the material deformation behavior with high precision at micrometer scales. These material

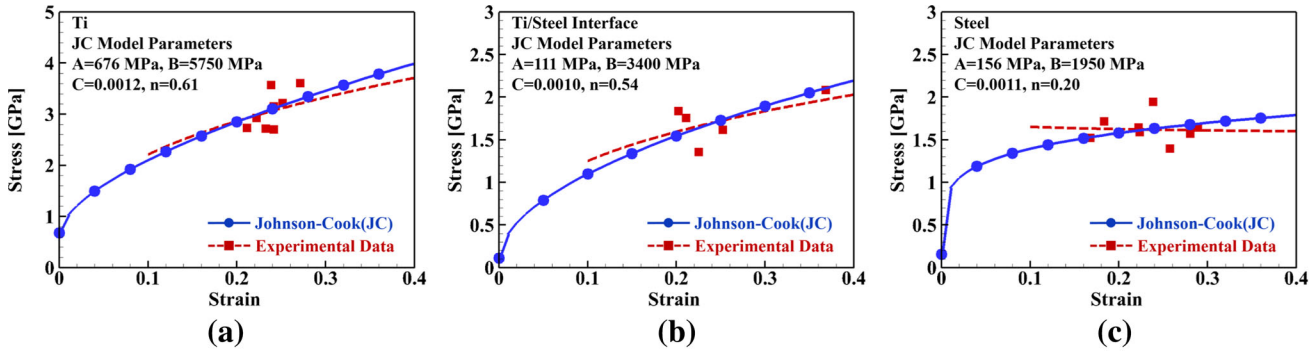

Fig. 11. Stress–strain response for (a) Ti, (b) Ti/steel interface, and (c) steel in dynamic indentation test at strain rate of 300 s^{-1}.

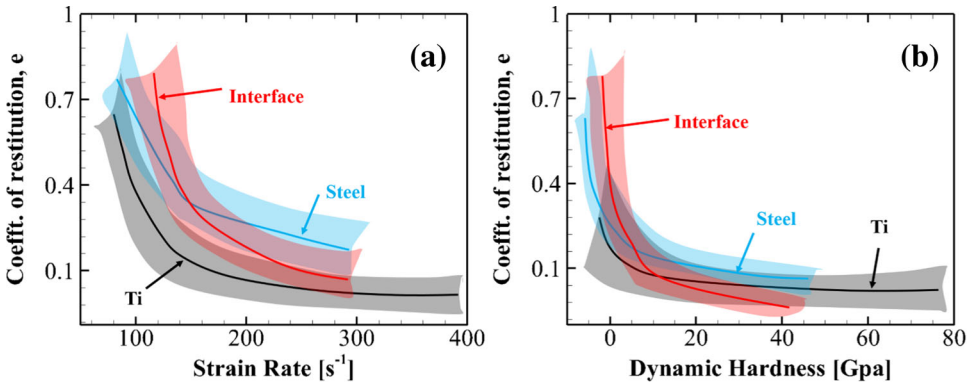

Fig. 12. Coefficient of restitution during impacts with (a) strain rate and (b) dynamic hardness.

parameters can be further used to describe the material behavior at the interface and in the homogeneous phases up to strain rates of $10^4\ s^{-1}$. All parameters are derived from the dynamic indentation experiments with high precision in the measurements and the locations of indentation as shown in Figs. 5 and 8. The temperature effect is neglected in the current analysis because all experiments are conducted at room temperature.

Dynamic Effects and Inelastic Impacts at Interfaces

An elastic–plastic material will reach the limit of elastic behavior at a point beneath the surface when the maximum contact pressure at the instant of maximum compression reaches the value 1.60 times of yield limit.[26] Up to the instant of maximum compression, the kinetic energy is absorbed in local deformation, elastic and plastic, of the two colliding bodies, i.e.:

$$\frac{1}{2}mV^2 = W = \int_0^{\delta} P\mathrm{d}\delta \tag{6}$$

After the point of maximum compression, the kinetic energy of rebound is equal to the work done during elastic recovery, thus:

$$\frac{1}{2}mV'^2 = W' = \int_0^{\delta} P'\mathrm{d}\delta' \tag{7}$$

We determine the maximum contact stress, the duration of the impact, and the coefficient of restitution (V'/V) in terms of the impact velocity V and the properties of the two bodies. Unfortunately, the compliance relationship for an elastic–plastic contact is not precisely defined, so that a theory of elastic–plastic impact is necessarily approximate because most impacts between metal bodies result in a fully plastic indentation we can concentrate on this regime. The coefficient of the restitution is calculated as:

$$e = \frac{V'}{V} \tag{8}$$

The coefficient of restitution is also very dependent on the hardness as well as the strain rate (Fig. 12). The coefficient of restitution drops at similar rate in the case of Ti and steel, but it drops at a much higher rate at the interface with the

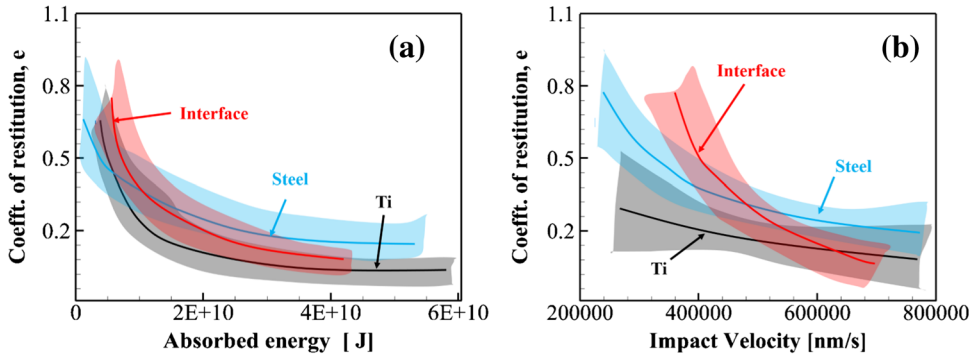

Fig. 13. Coefficient of restitution as a function of (a) absorbed energy and (b) impact velocity at the interface and the outside regions during impacts.

increase of hardness and strain rate. This is due to the fact that at higher strain rates, interface deforms as a higher rate. These effects are not present in the bulk phase, but in the interface region there is a mismatch of the elements and it shows higher impact depths with less energy available for rebounds thus exhibiting lower value of coefficient of restitution. At sufficiently low velocities, the deformation is elastic and the coefficient of restitution e is very nearly equal to unity (Fig. 13b). The absorbed energy is higher at lower coefficients of restitution, which also justifies the lower rebound velocities from the regions of higher hardness (Fig. 13a).

The interface region properties are highly dependent on the joined phases, the interlayer, and the processing temperatures and pressures, but this analysis also suggests that that the variation in the interface regions can be very well captured with the observations of strain-rate-dependent properties of the material. To fully characterize the interfaces properties, not only the mismatch in the parameters such as coefficient of thermal expansion and diffusion coefficient should be considered but also interface stress discontinuities and transversal stress effects should be considered.

CONCLUSION

Dynamic indentation-based small-scale impact experiments were performed on solid diffusion-bonded Ti/steel. The EDX analysis was performed postindentation to verify the impact sites, and elemental maps of the sites were obtained to show the diffusion region at the interfaces. The conclusions of the dynamic tests are as follows:

1. The dynamic hardness as a function of strain rate and stress rate shows different trends of the interface strength compared with the bulk phases.
2. The correlation coefficients among dynamic, strain rate, stress rate, plastic depth, residual depth, and absorbed energy during impacts show that bulk phases have the similar correlations but the interface regions have varying trends.
3. The JC model is fitted to the stress–strain data to find the material parameters to define the deformation behavior of the material with an account of inhomogeneity in the structure at the interface and nearby regions at high strain rates.
4. The coefficient of restitution is plotted with strain rate and dynamic hardness, showing that the material exhibits significant softening at higher strain rates.

These results show the need to better address the constitutive behavior of the interfacial regions, and the nanoimpact tests used in the current paper serve as an excellent tool to characterize the interfaces.

ACKNOWLEDGEMENTS

The authors express their sincere thanks to the excellent technical assistance of Dr. Christopher J. Gilpin, Chia-Ping Huang, and Laurie Mueller with the scanning electron microscopy at Purdue University. I would also like to thank my colleagues Dr. Ming Gan, Dr. You Sung Han, Dr. Hongsuk Lee, Tao Qu, and Yang Zhang for helpful discussions and Sudipta Biswas for being an extremely nice neighbor. This research is supported by NSF Grant CMMI1121113.

REFERENCES

1. B.D. Beake, S.R. Goodes, J.F. Smith, and F. Gao, *J. Mater. Res.* 19, 237 (2004).
2. D. Steinberg, S. Cochran, and M. Guinan, *J. Appl. Phys.* 51, 1498 (1980).
3. G.R. Johnson and W.H. Cook, *Paper presented at the Proceedings of the 7th International Symposium on Ballistics* (The Netherlands, 1983), p. 541.
4. F.J. Zerilli and R.W. Armstrong, *J. Appl. Phys.* 61, 1816 (1987).
5. D. Steinberg and C. Lund, *J. Appl. Phys.* 65, 1528 (1989).
6. D. Chichili, K. Ramesh, and K. Hemker, *Acta Mater.* 46, 1025 (1998).
7. W.-S. Lee and C.-F. Lin, *Mater. Sci. Eng. A* 241, 48 (1998).
8. G. Constantinides, C. Tweedie, N. Savva, J. Smith, and K. Van Vliet, *Exp. Mech.* 49, 511 (2009).
9. S. Kundu, S. Sam, and S. Chatterjee, *Mater. Sci. Eng, A* 560, 288 (2013).

10. K. Grandfield, A. Palmquist, and H. Engqvist, *Ultramicroscopy* 127, 48 (2013).
11. S. Sam, S. Kundu, and S. Chatterjee, *Mater. Des.* 40, 237 (2012).
12. S. Kundu, M. Ghosh, A. Laik, K. Bhanumurthy, G. Kale, and S. Chatterjee, *Mater. Sci. Eng. A* 407, 154 (2005).
13. S. Kundu, M. Ghosh, and S. Chatterjee, *Mater. Sci. Eng. A* 428, 18 (2006).
14. S. Kundu and S. Chatterjee, *Mater. Charact.* 59, 631 (2008).
15. A. Elrefaey and W. Tillmann, *J. Mater. Process. Technol.* 209, 2746 (2009).
16. S. Kundu, S. Sam, and S. Chatterjee, *Mater. Des.* 32, 2997 (2011).
17. S. Kundu, S. Sam, and S. Chatterjee, *Mater. Sci. Eng. A* 528, 4910 (2011).
18. S. Kundu, D. Roy, S. Chatterjee, D. Olson, and B. Mishra, *Mater. Des.* 37, 560 (2012).
19. P. Li, J. Li, J. Xiong, F. Zhang, and S.H. Raza, *Mater. Charact.* 68, 82 (2012).
20. S. Kundu, B. Mishra, D. Olson, and S. Chatterjee, *Mater. Des.* 51, 714 (2013).
21. X. Wang, Y. Yang, X. Luo, W. Zhang, G. Zhao, and B. Huang, *Intermetallics* 36, 127 (2013).
22. M. Gan and V. Tomar, *ASME J. Nanotechnol. Eng. Med.* 5, 021004 (2014).
23. M. Gan and V. Tomar, *AIP J. Appl. Phys.* 116, 073502 (2014).
24. M. Gan and V. Tomar, *AIP Rev. Sci. Instrum.* 85, 013902 (2014).
25. D. Verma, T. Qu, and V. Tomar, *JOM* 67, 858 (2015).
26. K.L. Johnson and K.L. Johnson, *Contact Mechanics* (Cambridge: Cambridge University Press, 1987).
27. H. Somekawa and C.A. Schuh, *J. Mater. Res.* 27, 1295 (2012).
28. J.W. Elmer, T.A. Palmer, and J. Wong, *J. Appl. Phys.* 93, 1941 (2003).
29. J.C. Bruhl, A.H. Varma, and W.H. Johnson, *Int. J. Impact Eng.* 75, 75 (2015).
30. P. Follansbee and U. Kocks, *Acta Metall.* 36, 81 (1988).
31. B. Xu and X. Chen, *J. Mater. Res.* 25, 2297 (2010).
32. L.H. He and M.V. Swain, *Dental Mater.* 23, 814 (2007).
33. G.T. Gray, *Ann. Rev. Mater. Res.* 42, 285 (2012).